

Electromagnetic Signatures of Neutron Star Mergers in the Advanced LIGO Era

Rodrigo Fernández^{1,2} and Brian D. Metzger³

¹Department of Physics, University of California, Berkeley, CA, 94720, USA

²Department of Astronomy & Theoretical Astrophysics Center, University of California, Berkeley, CA, 94720, USA

³Columbia Astrophysics Laboratory, Columbia University, New York, NY, 10027, USA

Ann. Rev. Nuc. Part. Sci. 2016. 66:1–24

This article's doi:
10.1146/(DOI)

Copyright © 2016 by Annual Reviews.
All rights reserved

First page note to print below
DOI/copyright line.

Keywords

neutron stars, gravitational waves, binaries, transients, nucleosynthesis

Abstract

The mergers of binaries containing neutron stars and stellar-mass black holes are the most promising sources for direct detection in gravitational waves by the interferometers Advanced LIGO and Virgo over the next few years. The concurrent detection of electromagnetic emission from these events would greatly enhance the scientific return of these discoveries. Here we review the state of the art in modeling the electromagnetic signal of neutron star binary mergers across different phases of the merger and multiple wavelengths. We focus on those observables which provide the most sensitive diagnostics of the merger physics and the contribution to the synthesis of rapid neutron capture (*r*-process) elements in the Galaxy. We also outline expected future developments on the observational and theoretical sides of this rapidly evolving field.

Contents

1. INTRODUCTION	2
2. INSPIRAL PHASE	4
2.1. Formation and Rates	4
2.2. Precursor Emission	4
3. DYNAMICAL PHASE	6
3.1. Overview of NSNS/NSBH merger evolution	6
3.2. Central remnant: prompt versus delayed BH formation	7
3.3. Dynamical ejecta	7
3.4. Accretion disk formation	8
4. ACCRETION PHASE	9
4.1. Short Gamma-Ray Burst Connection	9
4.2. Late Disk Evolution and Outflows	11
5. <i>r</i> -PROCESS NUCLEOSYNTHESIS AND ITS SIGNATURE (KILONOVA)	14
5.1. <i>r</i> -Process Nucleosynthesis in NS Mergers	14
5.2. Kilonova	16
5.3. Fast Ejecta and the Neutron Precursor	18
5.4. Non-Radioactive Energy Sources	19
5.5. Radio Transient from Ejecta Interaction with the Interstellar Medium	19

1. INTRODUCTION

Observations of the Hulse-Taylor binary pulsar (1) and of the double pulsar J0737-3039 (2) have proven the existence of gravitational waves (GWs). However, their direct detection remains elusive. This situation is anticipated to change soon, as a network of new GW observatories, including Advanced LIGO (3) (hereafter aLIGO), Advanced Virgo (4), and the Japanese cryogenic detector KAGRA (5), begin taking data over the next few years. The first detection of GWs will test a key prediction of General Relativity (GR) and mark the beginning of a new field: GW Astronomy.

Among the most likely sources to be detected in this initial phase are coalescing binaries containing two neutron stars (NS), hereafter NSNS mergers, or a NS and a black hole (BH), hereafter NSBH mergers (6)¹. These detectors are most sensitive to GWs from the late stages of the binary inspiral. At design sensitivity, aLIGO will be capable of detecting NSNS mergers out to an orientation-averaged distance ~ 200 Mpc, and NSBH mergers to a distance $\approx 2 - 3$ times larger (6). The planned network of GW interferometers can narrow down the location of a source using triangulation, but depending on the signal to noise ratio the final uncertainty can still be tens or hundreds of square degrees, translating into large uncertainties in the parameters inferred from the GW waveform [e.g., (8)].

Astronomers have refined the measurement of electromagnetic (EM) waves for centuries, and optical, near-infrared (IR), and many radio observatories have exquisite localization precision (\sim arcseconds) compared with GW observatories. For this reason alone, the detection of an EM counterpart to a GW source would greatly improve the quality of the information available from the GW data. It could also provide complementary information, such as the energetics and host galaxy of the event, and when (or whether) an event horizon

¹We do not consider double BH binaries here, see e.g. (7) for a review.

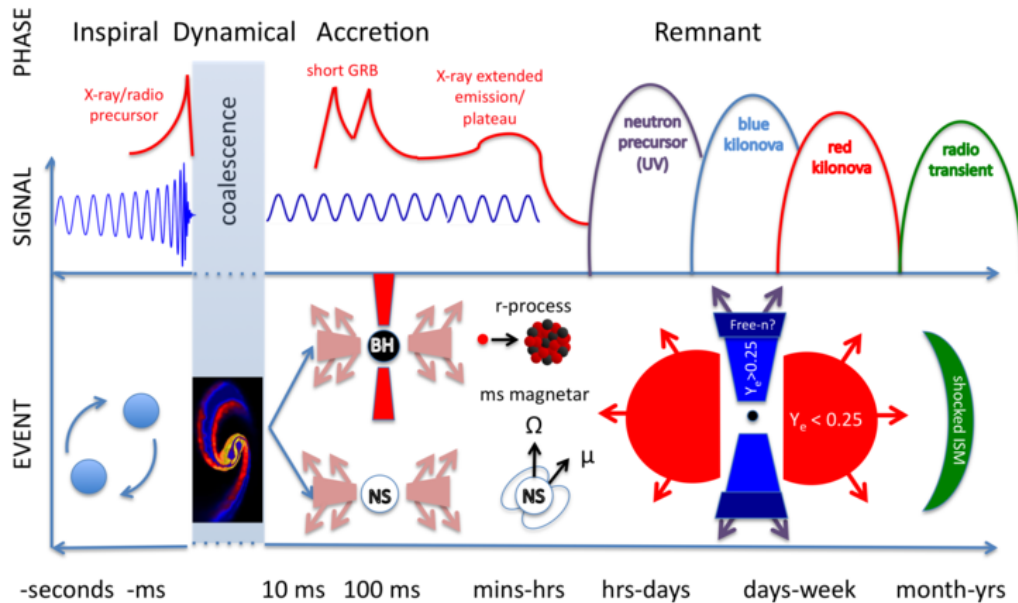


Figure 1

Phases of a neutron star merger as a function of time, showing the associated observational signatures and underlying physical phenomena. Coalescence inset courtesy of D. Price and S. Rosswog [see also (15)].

forms. Obtaining an accurate source position is multiplicative, as it enables a much larger range of electromagnetic facilities (often more sensitive, but with narrower fields of view, e.g. the Hubble Space Telescope) to obtain complementary observations.

Due to their transient nature, discovering the EM counterparts of NSNS/NSBH mergers requires follow-up observations with time-sensitive facilities. NASA's *Swift* and *Fermi* satellites provide nearly continuous coverage of the sky at hard X-ray and gamma-ray wavelengths. Several optical/IR transient surveys have been in operation over the last several years, with more coming online in the next several years, culminating in the Large Synoptic Survey Telescope (9). Wide-field radio arrays, such as LOFAR (10), provide nearly continuous coverage of the northern hemisphere sky in the hundreds of MHz radio band.

NSNS/NSBH mergers also represent an important topic in Nuclear Astrophysics. The neutron star equation of state (EOS) plays an important role in the GW signal, both during the late inspiral phase and in the fate of the post-merger remnant. The ejecta from NS mergers are an astrophysical source of rapid neutron-capture (*r*-process) nuclei, the origin of which has remained a mystery for almost 70 years (11, 12). The short-lived, neutron-rich nuclei produced during the *r*-process serve as probes of the nuclear force in asymmetric conditions and of the limits of nuclear stability (13). Significant efforts are underway to improve experimental capabilities to measure the masses and lifetimes of these nuclei, including the Facility for Rare Isotope Beams (14).

This review summarizes the state-of-the-art in the predicted EM emission from NSNS and NSBH mergers. The structure of the paper follows the time evolution of the merger

event, as shown in **Figure 1**. Future issues are summarized at the end of the article. Due to space constraints, we are not able to cover and/or cite all the work in the field; we refer the reader to other excellent reviews on this topic (16, 17, 18).

2. INSPIRAL PHASE

2.1. Formation and Rates

The GW detection rates of NSNS/NSBH mergers are uncertain due to their poorly constrained volumetric rate in the local universe. Ten NSNS binary systems are currently known in our Galaxy, of which 6 will coalesce within a Hubble time [Table 2 of (19)]. This population provides an empirically-calibrated estimate of the NSNS rate per stellar mass (20), which when translated to the Galaxy population as a whole results in an aLIGO/Virgo detection rate of 3-18 yr^{-1} (21). This estimate is, however, subject to several uncertainties, such as the faint end of the pulsar luminosity function and small number statistics (the rates are dominated by J0737-3039, which has a particularly short inspiral time).

No NSBH binaries are currently known, so the empirical method cannot be applied to estimate their rates. An upper limit is set by the galactic formation rate of High Mass X-ray Binaries (HMXBs) of $\sim 10^{-3} \text{ yr}^{-1}$, which when combined with the fraction of those which pass through a bright X-ray phase of a few percent, results in a rate of less than a few dozen NSBH mergers detected per year by aLIGO (22).

Population synthesis models [e.g., (23, 22, 24)] provide independent estimates of the NSNS and NSBH merger rates. For instance, Dominik et al. (24) predicts NSNS + NSBH detection rates of $\approx 3 - 7 \text{ yr}^{-1}$ for aLIGO/Virgo, consistent with the empirical estimates above. However, the full range of rates provided in the literature varies by several orders of magnitude [e.g., (6, 22)], due to the large uncertainties in the physics of binary evolution, such as the treatment of common envelope evolution, wind mass-loss from high mass stars, the evolution of metallicity with redshift, and supernova NS kicks.

NSNS rate calculations usually neglect the influence of external stellar interactions on the evolution of binaries, as justified for the vast majority of stars. In dense stellar environments, however, such as globular clusters or young stellar clusters, dynamical interactions may enhance the assembly rate of tight NS binaries [e.g., (25, 26)]. Additional theoretical uncertainties arise in estimating merger rates in this case due to the poorly constrained evolution of dense stellar systems. A key aspect of dynamically captured binaries is their potential to merge while the binary orbit still possesses high eccentricity [e.g., (27, 28)]. Although this channel likely represents a small fraction of all mergers (26), even a subdominant population of such events could be of outsized importance to r-process production and kilonova emission (§5.2), given the larger ejecta mass from eccentric mergers (28).

2.2. Precursor Emission

Compared to the post-merger phase, little study has been dedicated to the EM emission during the late inspiral phase prior to coalescence. If at least one NS is magnetized, then the orbital motion of the conducting companion NS or BH through its dipole magnetic field induces a strong voltage and current along the magnetic field lines connecting the two objects [e.g., (29, 30, 31, 32)]. This voltage accelerates charged particles, potentially powering electromagnetic emission that increases in strength as the orbital velocity increases and the binary separation decreases approaching merger.

Lai (33) shows that the power dissipated by this process is capped by the maximum current which can be sustained before the toroidal magnetic field induced by the current becomes comparable to that of the original poloidal dipole field. This is because the magnetic pressure of the toroidal field causes the magnetosphere to inflate, tearing open the field lines and disconnecting the circuit. As an alternative derivation of this maximum power, consider that the Poynting luminosity of a rotating magnetized NS is given by (34),

$$L_P = \left(\frac{f_\Phi}{\tilde{f}_\Phi}\right)^2 \frac{\mu^2 \Omega^4}{c^3} \approx 2 \times 10^{46} \text{ erg s}^{-1} \left(\frac{f_\Phi}{\tilde{f}_\Phi}\right)^2 \left(\frac{B_d}{10^{13} \text{ G}}\right)^2 \left(\frac{R_{\text{ns}}}{12 \text{ km}}\right)^6 \left(\frac{P}{\text{ms}}\right)^{-4}, \quad (1)$$

where $\mu \equiv B_d R_{\text{ns}}^3$, B_d , R_{ns} , and $\Omega = 2\pi/P$ are the dipole moment, surface equatorial dipole field, radius, and rotation rate of the NS, respectively. Here f_Φ is the fraction of the magnetic flux threading the NS surface which opens to infinity, normalized to its value,

$$\tilde{f}_\Phi = \int_0^{\theta_L} \sin \theta d\theta = [1 - \cos \theta_L] \approx \theta_L^2 \approx \frac{R_{\text{ns}}}{2R_L} \approx 0.13 \left(\frac{R_{\text{ns}}}{12 \text{ km}}\right) \left(\frac{P}{\text{ms}}\right)^{-1}, \quad (2)$$

for an isolated dipole, where $\theta_L \approx \sin^{-1}(R_{\text{ns}}/R_L)^{1/2}$ is the polar latitude of the last closed field line, which intersects the equatorial plane at the light cylinder radius $R_L = c/\Omega$.

Neglecting NS spin, equation (1) can be applied to the case of an orbiting conducting companion by replacing the spin frequency Ω with the orbital frequency, $\Omega_{\text{orb}} = (8GM_{\text{tot}}/a^3)^{1/2}$, where a is the binary separation. The open fraction f_Φ is reduced by a factor of $\approx 2R_c/(2\pi a)$ to account for the azimuthal angle subtended by the binary companion, and increased by a factor of $\approx R_L/a = c/(a\Omega_{\text{orb}})$ because field lines crossing the equatorial plane exterior to the binary separation a (instead of the light cylinder radius) are now open. Substituting $f_\Phi/\tilde{f}_\Phi \approx R_c c/(\pi\Omega_{\text{orb}} a^2)$ into equation (1) results in

$$L_P \approx \frac{8\mu^2 GM_{\text{tot}} R_c^2}{\pi c a^7} \approx 3 \times 10^{46} \text{ erg s}^{-1} \left(\frac{B_d}{10^{13} \text{ G}}\right)^2 \left(\frac{M_{\text{tot}}}{2M_{\text{ns}}}\right) \left(\frac{R_c}{R_{\text{ns}}}\right)^2 \left(\frac{a}{2R_{\text{ns}}}\right)^{-7}, \quad (3)$$

where in the numerical estimate we take $M_{\text{ns}} = 1.4M_\odot$ and $R_{\text{ns}} = 12 \text{ km}$. Equation (3) matches that estimated by (33) to within a factor of a few. The orbital decay time via GW emission is $t_{\text{GW}} \equiv a/\dot{a} \approx 5c^5 a^4/(128G^3 M_{\text{ns}}^3) \approx 5(a/2R_{\text{ns}})^4 \text{ ms}$, such that the maximum energy released as the orbit decays to separation a is given by

$$E_{\text{tot}} = \int^a L_P \frac{da}{\dot{a}} \approx \frac{5\mu^2 c^4 R_c^2}{24\pi G^2 M_{\text{ns}}^2 a^3} \approx 5 \times 10^{43} \text{ erg} \left(\frac{B_d}{10^{13} \text{ G}}\right)^2 \left(\frac{a}{2R_{\text{ns}}}\right)^{-3} \quad (4)$$

This radiation, if thermalized, will likely emerge at hard X-ray/gamma-ray frequencies, possibly resembling a GRB of duration $\sim t_{\text{GW}} \sim 1 - 10 \text{ ms}$. However, for magnetic fields of $\lesssim 10^{13} \text{ G}$ characteristic of radio pulsars, the resulting energy release of $E_{\text{tot}} \lesssim 10^{44} \text{ ergs}$ up to the point of merger ($a = 2R_{\text{ns}}$) is many orders of magnitude smaller than the measured luminosities of short GRBs, events believed to be produced in the merger aftermath (§4.1).

Particles accelerated by magnetospheric interaction could also give rise to a short burst of coherent radio emission (30), perhaps similar to the recently discovered class of events known as ‘‘fast radio bursts’’ (35). A low frequency radio precursor could arrive with delay of several seconds or longer after the GWs due to the subluminal group velocity of radio waves through the ionized plasma of the Galactic halo and intergalactic medium.

In addition to magnetospheric interaction, tidal resonant excitation of modes in the NS crust provides an additional wave to tap into the orbital energy of the merging binary. If driven to non-linear amplitudes, such modes shatter the crust, releasing $\approx 10^{46} - 10^{47} \text{ ergs}$ up to tens of seconds prior to merger, potentially producing an observable flare (36).

3. DYNAMICAL PHASE

The dynamical phase begins when tidal effects become important, and ends when the central remnant has settled into a stationary configuration. The outcome determines the subsequent evolution of the remnant and its EM counterparts. Since the changes in the gravitational potential over an orbit become non-linear, time-dependent simulations are required to answer both qualitative and quantitative questions.

Our understanding of this phase has developed through two parallel approaches: simulations using realistic microphysics with approximate gravity, originally aimed at assessing NSNS/NSBH mergers as progenitors of short gamma-ray bursts and nucleosynthesis sites, and models that employ full-GR and an approximate description of matter, aimed initially at generating reliable GW predictions. Each approach has contributed with key insights, and their tracks are gradually converging.

A number of recent review articles focus on the dynamical aspects of NSNS/NSBH mergers, primarily from a numerical relativity perspective (37, 38, 39, 7). Here we provide a brief overview of the key aspects that affect the prediction of EM counterparts and nucleosynthesis.

3.1. Overview of NSNS/NSBH merger evolution

The final product of the merger is always a central object that contains most ($\gtrsim 90\%$) of the mass initially in the binary system (§3.2). Matter can be ejected on a dynamical time, either by tidal forces and/or by compression at the interface between objects (§3.3), while the remaining material can possess enough angular momentum to circularize into an accretion disk (§3.4).

For quasi-circular NSNS mergers, the key parameter controlling the global evolution is the binary mass ratio. For nearly equal-mass NSs, the stars deform into symmetric teardrop shapes, with relatively small spiral arms, whereas for very unequal masses the lighter star is tidally disrupted by the more massive companion, forming a large spiral arm [e.g., (40)]. For large eccentricities the dynamics becomes more complex, with one or multiple close encounters before merger, in which matter can be exchanged and oscillations can be excited due to tidal interactions (41).

For NSBH mergers with small eccentricity, the key parameter is the ratio of the NS tidal disruption radius to the position of the innermost stable circular orbit (ISCO) of the system, which depends on the mass ratio, the BH spin and the NS radius [e.g., (38, 42)]. If the tidal radius sits inside the ISCO radius, the NS is swallowed whole by the BH and no mass ejection occurs. Otherwise, the neutron star is tidally disrupted, leading to the formation of long and narrow spiral arms (**Figure 2**). High eccentricity also increases the complexity of the dynamics (43).

Magnetic fields do not appear to have a significant effect on the global dynamics and gravitational waveform during the inspiral and merger [e.g., (44)]. Instead, they become important in the subsequent evolution of the merger remnant (§3.2). It has been known for a decade (15) that strong field amplification can occur at the shearing interface of NSNS mergers. However, the stringent resolution requirements demanded by the instabilities involved (45) are beyond current computing capabilities for global simulations under realistic conditions.

3.2. Central remnant: prompt versus delayed BH formation

The maximum mass of a cold, non-rotating neutron star, set by the EOS of dense matter, can be increased by rotational and thermal support [e.g., (46)]. The remnant of a NSNS merger absorbs a significant fraction of the angular momentum in the binary, and gains thermal energy via shocks. The non-collapsed, differentially-rotating object is generally called a hypermassive neutron star (HMNS). In the case of a NSBH merger, the remnant is always a BH.

The fate of the HMNS depends primarily on the total mass of the binary (47). Above a threshold value, a BH forms on a dynamical time (\sim ms). This critical mass is EOS-dependent, and covers the range $\sim 2.6\text{--}3.9M_{\odot}$ for soft and stiff nuclear-theory based EOSs, respectively, with empirical relations connecting the threshold mass with EOS parameters [e.g., (48, 49)].

If collapse is not prompt, then the lifetime of the HMNS is determined by a number of processes: angular momentum transport via hydrodynamic torques, gravitational waves [e.g., (50)] or the magnetorotational instability (MRI) [e.g., (51, 52)], and loss of thermal energy via neutrino emission (53). Support against gravity is eventually lost, with the possible exception of the merger of two low-mass NSs. The characteristic timescales for angular momentum transport by the MRI and neutrino cooling are $\sim 10\text{--}100$ ms and $\sim 1\text{--}10$ s, respectively [e.g., (54)], while loss of uniform rotational support for a HMNS slightly above the maximum mass can occur over a much longer spin-down timescale. Determining which process is dominant remains an active area of research.

The lifetime of the HMNS is key for the qualitative form of the post-merger GW emission. Prompt BH formation leads to a rapid decrease of the waveform amplitude (a ‘ring-down’), while a surviving HMNS generates strong peaks in the GW spectrum in the frequency range $2\text{--}4$ kHz due to sustained global oscillations [e.g., (55)]. The information contained in these spectral peaks can be used to set constraints on the EOS of dense matter (56), although aLIGO-type interferometers will only be able to detect them out to few tens of Mpc. An alternative diagnostic of the HMNS lifetime is the color of the kilonova (§5.2).

3.3. Dynamical ejecta

The merger gives rise to unbound matter ejection through processes that operate on the dynamical time, and which depend primarily on the total binary mass, the mass ratio, and the EOS. Ejected masses lie in the range $10^{-4}\text{--}10^{-2}M_{\odot}$ for NSNS mergers [e.g., (57)], with velocities $0.1\text{--}0.3c$. For NSBH mergers, the ejecta can be up to $\sim 0.1M_{\odot}$, with similar velocities [e.g., (58)]. More mass can be ejected if the eccentricity is large (41, 28).

Two main mass ejection processes operate in NSNS mergers. First, material at the contact interface is squeezed out by hydrodynamic forces and is subsequently expelled by quasi-radial pulsations of the remnant (59, 57, 40), ejecting shock-heated matter in a broad range of angular directions (Figure 2). The second process involves spiral arms from the non-axisymmetric HMNS, which expand outwards – primarily on the equatorial plane – due to angular momentum transport by hydrodynamic processes. The relative importance of these mechanisms depends on the EOS: a more compact configuration enhances ejection from the contact interface (40). The mass ratio also influences the ejected mass, with very asymmetric binaries generating up to about twice the material as a symmetric binary of the same total mass (40). The total mass also affects the system through the BH formation timescale: for prompt collapse, ejection from the contact interface is suppressed due to

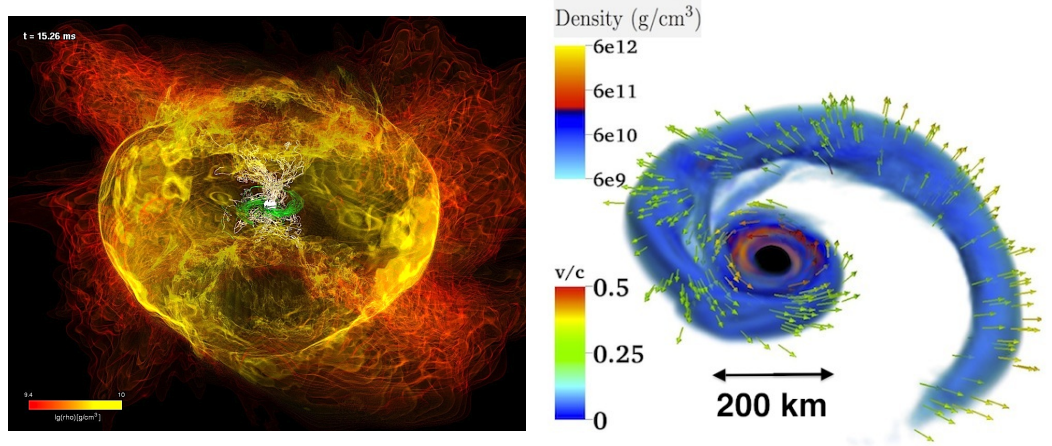


Figure 2

Three-dimensional visualizations of the post-merger ejecta. *Left*: Density field from an equal-mass NSNS merger, with magnetic field lines shown in green [from Rezzolla et al. (60), ©AAS, reproduced with permission]. The ejecta has significant components in most angular directions (§3.3). *Right*: Density rendering from a NSBH merger with mass ratio 1.2/7 [from Foucart et al. (61), ©American Physical Society]. The ejecta is confined to the equatorial plane because it is generated primarily by tidal forces.

prompt swallowing of this region. Symmetric binaries above the threshold mass yield some of the lowest dynamical ejecta masses ($\sim 10^{-4}M_{\odot}$) (57).

Regarding NSBH mergers, the primary mechanism of mass ejection is the tidal force that disrupts the NS on the equatorial plane via angular momentum redistribution [e.g., (57)]. The geometry of the ejecta is thus fundamentally different from that of NSNS mergers, as Figure 2 illustrates. Also, the ejecta from NSBH mergers often covers only part of the azimuthal range (58). This has important implications for the properties of the radioactively-powered electromagnetic counterparts (§5.2).

The thermodynamic properties of the dynamical ejecta can depend sensitively on the microphysics employed and the treatment of neutrinos, particularly for NSNS mergers. Studies in full GR with all these components have only recently been performed, remaining an active area of research [e.g., (62, 63)].

3.4. Accretion disk formation

Ejected material that is not gravitationally unbound from the central remnant either falls back or circularizes into an accretion disk. The disk mass depends primarily on the mass ratio of the binary, and on the spins of the binary components, the EOS, and the total binary mass [e.g., (59, 38)]. For quasi-circular NSNS and NSBH mergers, disk masses can reach up to $\sim 0.3M_{\odot}$ [e.g., (59, 64, 61)], with a similar range obtained for large eccentricities (43, 41).

In NSNS mergers, the material that forms the disk comes from the contact interface and the tips of the spiral arms (65). The disk mass appears to be particularly sensitive to the development of a primary spiral arm, with a corresponding sensitivity to the mass ratio (59). The spins of the NS enter through the total angular momentum in the pre-merger

binary: co-rotating spins yield larger disk masses than irrotational binaries (59). A stiffer EOS (larger NS radius for fixed mass) leads to more efficient tidal disruption for asymmetric binaries, and hence to larger spiral arms and thus higher disk mass (59). The total binary mass influences the disk through the BH formation time: prompt collapse quickly swallows mass from regions that would otherwise end up as disk material (66). The lowest disk masses ($\sim 10^{-4}M_{\odot}$) are obtained for symmetric binaries above the threshold for prompt BH formation (57). In contrast, a longer-lived HMNS can transfer angular momentum outwards via dynamical torques for a sustained period, leading to a larger disk mass [e.g., (64)].

Regarding NSBH mergers, the disk forms when the tidally-stretched neutron star wraps around and intersects itself [e.g., (38)], with the possible exception of systems with precession. Despite the presence of shocks, a one-armed spiral structure persists for many orbits in the disk, transporting angular momentum and generating accretion onto the BH [e.g., (58)]. In addition to the dependence on the stiffness of the EOS as in NSNS mergers, the disk mass also increases for larger spin in the initial BH.

4. ACCRETION PHASE

Once a few dynamical times have elapsed, the gravity of the central remnant settles into a stationary form and the subsequent evolution of the system occurs on longer timescales.

4.1. Short Gamma-Ray Burst Connection

4.1.1. Observational Connection. Gamma-ray bursts (GRBs) are luminous and highly variable flashes of \sim MeV γ -rays. Long-duration GRBs, usually defined as those lasting longer than 2 seconds, are associated with the core-collapse of massive stars [e.g., (67)]. Short-duration GRBs (SGRBs) last less than two seconds and are characterized by spectrally harder emission. Their origin is poorly understood compared to long bursts, due in part to their dimmer afterglows, which makes them more challenging to localize.

GRBs are produced by internal dissipation and non-thermal emission within a collimated ultra-relativistic outflow, or ‘jet’. Their rapid variability and enormous isotropic-equivalent luminosities of $L_{\gamma} \sim 10^{50} - 10^{52}$ erg s $^{-1}$ demand that GRB jets be powered by rotational or gravitational energy released from a solar mass compact object. This energy release could occur through the accretion of a massive torus on the characteristic accretion (“viscous”) timescale

$$t_{\text{visc}} \sim \frac{R^2}{\nu} \approx 0.26 \text{ s} \left(\frac{\alpha}{0.1} \right)^{-1} \left(\frac{R}{30 \text{ km}} \right)^{3/2} \left(\frac{M_{\text{BH}}}{3M_{\odot}} \right)^{1/2} \left(\frac{H}{0.1R} \right)^{-2}, \quad (5)$$

where R is the characteristic radial extent of the torus, $\nu = \alpha c_s H$ is the effective viscosity due to turbulence within the disk, c_s is the midplane sound speed, and $H \approx c_s / \Omega_K$ is the vertical scale-height of the disk, with $\Omega_K = (R^3 / GM_{\text{BH}})^{1/2}$ the Keplerian orbital frequency around a BH of mass M_{BH} .

For NSNS/NSBH mergers, we expect $M_{\text{BH}} \sim 3 - 20M_{\odot}$, $R \sim$ tens of km, such that $t_{\text{visc}} \sim 0.1 - 1$ s for a range of physical viscosities $\alpha \sim 0.01 - 0.1$. The correspondence between t_{acc} and the observed durations of SGRBs provides suggestive evidence for a link between SGRBs and NSNS/NSBH mergers (68, 69). Additional observational support of the SGRB-merger connection includes [e.g., (17)]: (1) an association with both spiral and elliptical host galaxies, consistent with the expected distribution of delay times between star

formation and NSNS/NSBH mergers; (2) a lack of bright coincident supernovae or other evidence of star formation, indicating a non-massive star origin; (3) a distribution of the observed spatial offsets of SGRBs from their host galaxy light which is consistent with that resulting from NS birth kicks (70, 71); and (4) the possible detection of kilonova emission following the SGRB 130603B [(72, 73), §5.2].

Equation (5) shows that producing a SGRB through accretion requires forming a massive, compact torus on a comparable timescale, disfavoring scenarios that would produce a more radially-extended disk, such as the collapse of a massive star. One model which can overcome this limitation is the accretion-induced collapse of a NS [e.g., (74)]. However, such an event is unlikely to leave a remnant disk outside of the BH horizon for NS properties consistent with observationally allowed EOSs (75).

4.1.2. Relativistic Jet Formation. The SGRB jet energy can be parameterized as $E_j = \epsilon_j M_t c^2 \approx 10^{50} (\epsilon_j/10^{-3}) (M_t/0.1M_\odot)$ erg, where M_t is the torus mass and ϵ_j is an efficiency factor. For a torus mass $M_t \sim 0.1M_\odot$ (§3.4), producing a GRB jet of the observed energy range of $E_\gamma \approx L_\gamma t_\gamma f_b \sim 10^{48} - 10^{51}$ erg requires only a modest efficiency factor $\epsilon_j \lesssim 10^{-5} - 10^{-2}$, where $f_b \sim 0.01 - 0.1$ is the uncertain beaming fraction that relates the true energy to that assuming isotropic emission based on the observed flux, and t_γ is the burst duration. In order to explain the high inferred jet Lorentz factors of $\Gamma \gtrsim 100$, this energy must furthermore be placed into a small quantity of baryonic mass $M_j \approx E_j/\Gamma c^2 \approx 10^{-7} - 10^{-5}M_\odot$.

The relatively low density of the polar region above the central remnant provides a natural location for jet launching. Two energy sources are usually considered. First, neutrinos from the accretion torus deposit a fraction of their energy along the polar axis via self annihilation, mainly $\nu_e - \bar{\nu}_e$ (76). This ‘high entropy’ jet is accelerated to relativistic velocities by thermal pressure, as in classical fireball models (68). The strength of this model is that annihilation heating must occur at some level. A weakness, however, is the low efficiency $\epsilon_j \lesssim 10^{-3}$, which furthermore peaks at the very earliest times after the merger, when the dense dynamical and wind-driven ejecta could inhibit jet formation (77, 78).

The jet could alternatively be powered by the Poynting flux from a strong magnetic field threading the rotating central compact object or the accretion disk. An MHD jet can in principle possess a much higher efficiency ($\epsilon_j \sim 1$), especially if the power source is the spin energy of the black hole (79). Dynamical simulations of NSNS/NSBH mergers have begun to explore magnetic field amplification following the merger [e.g., (80), see also §3.1] with some showing the formation of a magnetic field topology conducive to jet formation (60, 81). This represents an important direction for future research.

After being launched near the central compact object, the jet may be collimated on larger scales by confinement provided by a dense external medium. This medium may be provided by the dynamical ejecta or accretion disk outflows (82, 83, 84).

4.1.3. Extended Emission and Millisecond Magnetar Remnants. Roughly one quarter of SGRBs are accompanied by temporally extended hard X-ray emission, which lasts for a minute or longer after the main burst (85). The rapid variability of this ‘‘extended emission’’ (EE) indicates that it is powered by on-going activity from the central engine, as opposed to the GRB afterglow at much larger radii. The total isotropic energy of the EE is comparable or exceeding that of the initial SGRB itself. Some SGRBs are also accompanied by X-ray afterglows that decay more slowly in time than predicted by synchrotron blast wave models

(86). The abrupt cut-off of this plateau-like emission in some cases is again challenging to explain with the afterglow, implying a central engine origin (86).

The EE and X-ray plateaus last much longer than the expected lifetime of the prompt accretion disk (eq. [5]), posing a challenge to standard NSNS/NSBH merger models. This activity could be powered by the accretion of marginally bound matter which falls back to the BH at late times [e.g., (87, 88)]. However, fall-back models require very low disk viscosities (88) or a magnetic field topology that plays a non-trivial role in the jet dynamics (89). Accretion disk outflows could also obstruct the fall-back material (90).

An alternative model postulates that the EE is powered by a rotating magnetized NS remnant, a ‘millisecond magnetar’. The discovery of $\sim 2M_{\odot}$ NSs [e.g., (91)] makes it likely that NSNS mergers produce meta-stable HMNS remnants (§3.2), if not NSs which are indefinitely stable to gravitational collapse [e.g. (92, 83, 93)]. The NS remnant is formed with a rotational period $P \sim 1$ ms and may acquire a strong magnetic field $\gtrsim 10^{14} - 10^{15}$ G via dynamo action (94). The NSNS merger remnant possesses a reservoir of rotational energy of $E_{\text{rot}} = I\Omega^2/2 \simeq 3 \times 10^{52} \text{erg} (P/1 \text{ms})^{-2}$, where $I \simeq 2 \times 10^{45} \text{g cm}^2$ is the NS moment of inertia, which can be extracted via magnetic dipole radiation (eq. [1]). If the remnant is initially supported by rotation, then once enough angular momentum is lost to EM emission or GWs, its resulting collapse to a BH could result in an abrupt decrease in the X-ray emission (86).

A transient relativistic jet could be powered by the remnant torus accreting onto the NS remnant (instead of a BH), in analogy with Galactic accreting NS systems with relativistic jets [e.g. Circinus X-1]. This scenario would naturally preserve the correspondence between the viscous timescale (eq. [5]) and the GRB duration. However, baryon contamination by the neutrino-driven wind (§4.2.2) could prevent the jet from becoming ultra-relativistic [e.g., (95)]. If most of the field lines threading the rotating NS pass through the accretion disk or a slower wider angle wind instead of the core of the jet, then the jet baryon loading would be correspondingly reduced. Until the interplay between neutrinos and the magnetic field is better understood in this complex, highly time-dependent environment, it may be premature to conclude that BH formation is necessary to produce a SGRB.

4.2. Late Disk Evolution and Outflows

4.2.1. Global evolution. The basic properties of neutrino-cooled accretion disks were established by (96) using steady-state models. For the relevant accretion rates, there is a near balance between heating by angular momentum transport and neutrino losses at small radii. At larger radii, where the temperature is lower, neutrino cooling becomes inefficient and the disk reaches the ‘advective’ regime (97). The transition occurs approximately where the viscous time [equation (5)] is equal to the neutrino cooling time ($T \sim 3$ MeV for $\alpha = 0.03$ and typical disk parameters). For high accretion rates ($\gtrsim 1M_{\odot} \text{s}^{-1}$), the disk becomes opaque to neutrinos and it also cools inefficiently [e.g., (98)].

The first time-dependent calculation that followed the disk evolution over several viscous times using a one-zone model (99) showed that as the disk evolves, it transitions from the neutrino-cooled stage to the advective state as it spreads and its temperature decreases. These results were confirmed by subsequent one-dimensional height-integrated models (100).

Multi-dimensional simulations were first carried out by (66) for a few orbits (~ 10 ms), solving the hydrodynamic equations in three-dimensions, with a physical EOS and a neutrino leakage scheme. Results showed that the basic expectations about neutrino opaqueness

Neutrino Signal.

Neutrino emission from NSNS/NSBH mergers is comparable to that from core-collapse supernovae, with peak luminosities $\sim 10^{53}$ erg s $^{-1}$ (106). The duration of this signal can vary. If a BH forms promptly, the emission is dominated by accretion and hence it decreases on a viscous time (equation 5), while a long-lived HMNS significantly increases the magnitude and duration of the signal.

The most optimistic rate of NSNS mergers from (6) yields one event per 1000 yr in the galaxy, or a factor at least ~ 10 lower than the core-collapse supernova rate. Current observatories can at best detect ~ 1 neutrino from a supernova in Andromeda (distance 780 kpc) (107). Hence it is unlikely that neutrino emission will be observed from a NSNS/NSBH merger before megaton-scale detectors become available.

and cooling efficiency from (96) were correct. Work by Lee et al. (101, 102) included for the first time angular momentum transport by an α viscosity, and carried out the evolution for a few viscous times (~ 1 s), showing that qualitative transitions in the evolution can occur depending on the relation between the viscous time and the neutrino cooling time. The three dimensional models of (103) also evolved the disk to a time ~ 400 ms and characterized the effect of viscosity and BH spin on the neutrino emission. Finally, the disk evolution in MHD has been computed to times ~ 100 ms by (104, 105).

4.2.2. Mass ejection by neutrino energy deposition. Duncan et al. (108) showed that when the neutrino temperature of a protoneutron star exceeds a threshold, a hydrostatic atmosphere is no longer possible and a thermally-driven wind is launched. Ruffert et al. (106) pointed out that this phenomenon could also occur in the remnants of NSNS/NSBH mergers, with neutron-rich material being ejected in this ‘neutrino-driven wind’. A series of papers by Surman, McLaughlin, and collaborators [e.g., (109)] used parameterized wind trajectories to explore r -process production in these outflows, with similar work carried out by (110, 111).

Time dependent models of remnant tori that include neutrino emission and absorption indicate that when a BH forms promptly, the amount of mass ejected through this channel is very small because the torus becomes transparent very quickly (103). Fernández & Metzger (112) evolved disks around BH for a time ~ 1 s, finding that neutrino energy deposition is dynamically unimportant compared to viscous energy deposition (§4.2.3). This result was confirmed by (113) using more advanced neutrino transport, with an estimated contribution to the total disk outflows of \sim few % due to neutrino heating alone.

If the HMNS can survive for longer than a thermal time in the inner disk (~ 50 ms), the larger neutrino luminosity [Figure 3, see also (114)] can lead to the ejection of non-negligible amounts of mass ($\sim 10^{-3}M_{\odot}$). This was first shown explicitly by (95) using two-dimensional simulations with neutrino transport, and has recently been revisited by (115) using three-dimensional simulations.

4.2.3. Late mass ejection in the advective state. Significant outflows can be driven on timescales longer than the thermal time once the bulk of the disk achieves the advective state, in which heating by angular momentum transport and nuclear recombination are unbalanced by neutrino cooling [e.g., (117)]. This state is accompanied by freezeout of weak

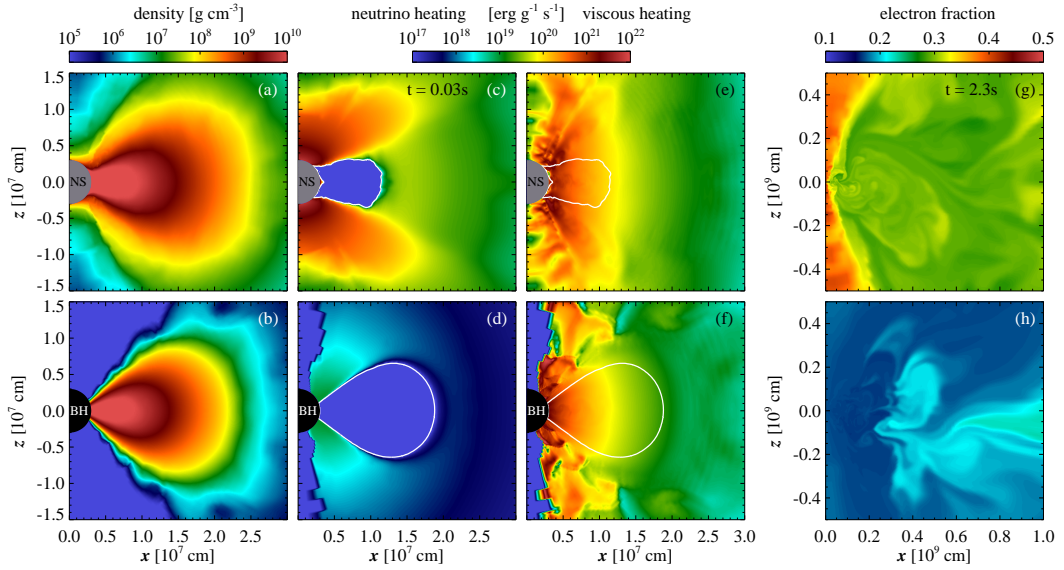


Figure 3

Snapshots in the evolution of NSNS/NSBH remnant accretion disks around a HMNS (top row) and BH (bottom row), highlighting the differences in key quantities. Columns show density, neutrino heating, and viscous heating at a time comparable to the thermal time in the disk (~ 30 ms), and the electron fraction at later times when the disk wind is underway (note the difference scale of the rightmost column). Figure from Metzger & Fernández (116).

interactions, leading to a neutron-rich wind (99, 100).

The work of (112) addressed the late-time evolution of the disk and its composition simultaneously, accounting for neutrino emission and absorption. Results showed that for a non-spinning BH, several percent of the initial disk mass are ejected on a timescale of ~ 1 s, and that the material is sufficiently neutron-rich ($Y_e \sim 0.2$) to produce heavy r -process elements. Just et al. (113) included two-moment neutrino transport and the effects of BH spin, finding more mass ejection (factor of several) when the BH spin has a more representative value $\chi \simeq 0.8$, with electron fractions as high as $Y_e \sim 0.35$.

A larger amount of mass ($\gtrsim 90\%$ of the initial disk mass) can be ejected when a long-lived HMNS sits at the center (116). The difference is related to the presence of a hard surface and the higher level of neutrino irradiation (Figure 3). This also leads to a higher average Y_e in the wind and thus to a variable composition that depends on the lifetime of the HMNS.

Currently, the largest theoretical uncertainty is the magnitude of the heating due to angular momentum transport. The work of (104, 105) has pioneered the use of MHD in this context, but the evolution was not long enough and the floor of density too high for the appearance of the late-time outflow.

The mass ejected by the late disk wind can be comparable to or larger than that in the dynamical ejecta. This is illustrated in **Figure 4**, where dynamical ejecta masses from several merger simulations are compared with estimates for the disk wind, assuming 10% of the initial disk mass.

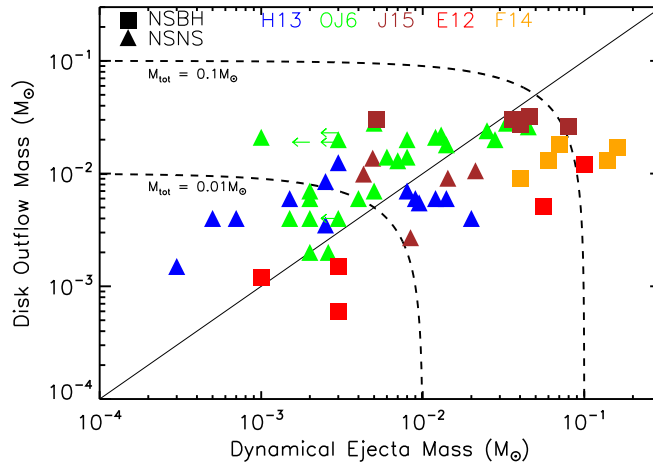


Figure 4

Mass ejected dynamically versus that ejected in disk outflows. Each point corresponds to the results of a single simulation, including the NSNS models of (57) (*blue triangle*), (65) (*green triangles*; upper limits are shown as arrows), (113) (*brown triangles*) and the NSBH models of (28) (*red squares*) and (61). The mass in disk outflows is estimated to be 10 per cent of the disk mass (§4.2.3). Dashed lines show a combined ejecta mass (dynamical + disk winds) of $\approx 0.1M_{\odot}$ and $0.01M_{\odot}$, showing the range necessary to explain the Galactic production rate of heavy r -process nuclei $\sim 5 \times 10^{-7}M_{\odot} \text{ yr}^{-1}$, given the allowed range of rates of NSNS mergers $\in [4, 61] \text{ Myr}^{-1}$ (99% confidence) as calculated based on the population of Galactic binaries (21).

5. r -PROCESS NUCLEOSYNTHESIS AND ITS SIGNATURE (KILONOVA)

In this section we briefly summarize the basic properties of r -process nucleosynthesis in NSNS and NSBH mergers, and the associated EM counterparts. Recent reviews on r -process nucleosynthesis can be found in (118, 119, 120), and on kilonovae and related EM emission in (121, 18). The reader should also consult the article by Arcones & Martínez-Pinedo in this volume.

5.1. r -Process Nucleosynthesis in NS Mergers

The rapid neutron capture process (r -process) was introduced to account for elements which require formation through neutron captures at rates faster than beta decays, given the properties of the nuclear chart and the Solar System abundance curve (11, 12). Approximately half of the elements heavier than Zinc ($Z = 30$) are thought to be generated through this channel [e.g., (119)].

The large neutron densities, high temperatures, and fast timescales required suggest an explosive environment. Core-collapse supernovae have been a leading candidate since the earliest r -process studies, with the neutrino driven wind phase becoming the focus as understanding of the explosion improved (122). Additional candidate sites include the jets of magnetorotational supernovae (123) and a neutrino-induced r -process in the He shells of massive stars at late times during core-collapse supernovae (124).

NSBH mergers were first suggested as a site for the r -process by Lattimer & Schramm

(125) by virtue of material ejected by the tidal disruption of the NS. They noted that the total yield from these events could match the amount of r -process elements observed in the Galaxy. Lack of knowledge about the dense matter EOS, the approximate calculation method, and uncertain statistics about the merger rates prevented more definitive statements. Significant progress had to wait more than 20 years: Freiburghaus et al. (126) ran a nuclear reaction network on tracer particles from Newtonian NSNS merger simulations with a physical EOS, finding good agreement with the solar system r -process abundances for suitable initial Y_e of the material.

5.1.1. Nucleosynthetic Yields . The dynamical ejecta from NSNS/NSBH mergers can be a robust generator of heavy ($A \gtrsim 140$) r -process elements. This robustness is rooted in ‘fission recycling’ [e.g., (127)]: the low initial Y_e results in a large neutron-to-seed ratio, allowing the nuclear flow to reach heavy nuclei for which fission is possible ($A \gtrsim 250$). The fission fragments are then subject to additional neutron captures, generating more heavy nuclei and closing the cycle.

The resulting abundance pattern follows the general shape of the r -process distribution in the Solar System and metal-poor halo stars, with abundances below $A \sim 140$ depleted (126). The quantitative agreement depends primarily on nuclear physics properties such as the nuclear mass model, fission fragment distribution, and β -decay half lives [e.g., (128)]. Other factors such as the EOS or binary parameters, while key for determining the amount of mass ejected (§3.3), have little influence on the abundance distribution (129, 130, 40), as illustrated in **Figure 5**.

Elements with $A \lesssim 140$ can also be generated in NSNS/NSBH mergers, although the yields are sensitive to astrophysical parameters. The late-time wind can synthesize elements in the entire r -process range due to its broad Y_e distribution (113). When combined with the dynamical ejecta, the ensemble distribution contains an intrinsic dispersion for $A \lesssim 140$, with a dependence on parameters such as the disk mass (Figure 5). In the case of a long-lived HMNS, the neutrino-driven wind is also a source of light r -process elements (131). Finally, recent work that includes neutrino absorption in dynamical merger simulations finds that irradiation from the HMNS can generate a broad Y_e distribution, leading to the entire range of r -process elements being generated by the dynamical ejecta alone (62).

5.1.2. Observational Constraints . By now it is well-established observationally that many old, metal-poor stars in the Galactic halo have inferred r -process element abundance distributions that closely follow the Solar System pattern for elements heavier than Ba ($Z \geq 56$), particularly at low metallicity [e.g., (119)]. This is taken as evidence for a robust r -process site that operated since early on in the life of the Galaxy.

One standard observational test to be met by any candidate site is the enrichment history of the Galaxy, as inferred from the Eu/Fe abundance ratio (relative to solar) as a function of metallicity in metal-poor halo stars. Recent studies that include realistic mixing processes in galaxy simulations (132, 133, 134) find reasonable agreement with the observations when assuming that NSNS/NSBH mergers are the dominant source of r -process enrichment.

Regarding light r -process elements, the abundance patterns inferred from metal-poor stars do not uniformly follow the Solar System, with a dispersion in the relative amounts of heavy and light elements [e.g., (119)]. NSNS/NSBH mergers are able to provide for light r -process elements through disk outflows, in amounts that have an intrinsic dispersion

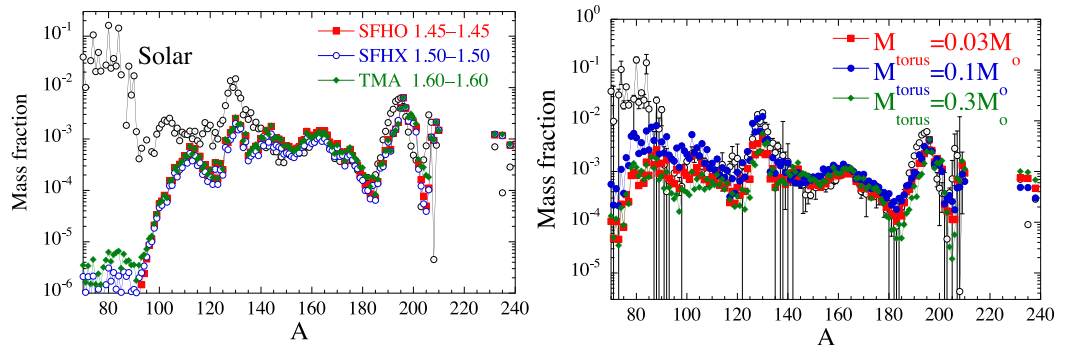


Figure 5

Left: Mass fractions synthesized during the expansion of the dynamical ejecta for three equal-mass, delayed-collapse NSNS merger models that employ different equations of state and total binary masses. Circles denote the Solar System r -process mass fractions. Note the low sensitivity of the abundances to binary parameters or EOS. *Right:* Combined mass fractions produced by the dynamical ejecta and disk wind for three disk masses, showing the dispersion in the abundance of elements with $A \lesssim 140$ due to the different disk masses. Figures from Just et al. (113), reproduced by permission of Oxford University Press on behalf of the Royal Astronomical Society

relative to heavier elements due to the sensitivity of the disk and dynamical ejecta masses to binary parameters (113). Current models of CCSNe nucleosynthesis also yield primarily light r -process elements in the neutrino-driven wind, contributing further to the diversity of light r -process element abundances in Galactic stars [e.g., (135)].

5.2. Kilonova

Nuclei freshly synthesized by the r -process are radioactive. As this expanding matter decays back to stability, the energy released via beta-decays and fission can power a thermal transient lasting days to weeks, commonly² known as a ‘kilonova’ (138, 137, 136, 139). Kilonovae are promising EM counterparts because their emission is approximately isotropic (compared to the beamed SGRB) and can peak at optical wavelengths, where sensitive searches are possible (121). Their brightness, duration, and colors are diagnostics of physical processes during the merger. Kilonovae also provide a unique probe to directly observe and quantify the production of r -process nuclei.

The basic properties of kilonovae are understood with a toy model (136). Approximate the ejecta at time t after the merger as a homogeneous sphere of mass M , uniform velocity v , radius $R \approx vt$, volume $V \approx 4\pi R^3/3$, and density $\rho = M/V$. As the ejecta expands, its thermal energy E evolves according to

$$\frac{dE}{dt} = \dot{E}_{\text{nuc}} - L - P \frac{dV}{dt} = \dot{E}_{\text{nuc}} - \frac{E}{t_{\text{diff}}} - \frac{E}{t}, \quad (6)$$

where the first term on the right hand side accounts for radioactive heating and the second term for radiation losses, where $t_{\text{diff}} = (3\kappa M)/(4\pi cvt)$ is the diffusion time and κ is the mean

²The term ‘kilonova’ was introduced by Metzger et al. (136), who first calculated light curves self-consistently using the radioactive heating of r -process nuclei. The term ‘macronova’ is also sometimes used (137).

opacity. The last term in equation (6) accounts for adiabatic losses, where $P = E/(3V)$ is the pressure in the radiation-dominated ejecta. The ejecta density is such that radiation can freely escape from the bulk only once the expansion time $t = R/v$ equals t_{diff} , i.e. after a ‘peak’ time

$$t_{\text{pk}} = \left(\frac{3\kappa M}{4\pi c v} \right)^{1/2} \approx 2.7 \text{ day} \left(\frac{M}{10^{-2} M_{\odot}} \right)^{1/2} \left(\frac{v}{0.1 c} \right)^{-1/2} \left(\frac{\kappa}{\text{cm}^2 \text{ g}^{-1}} \right)^{1/2} \quad (7)$$

The opacity is dominated by Doppler-broadened atomic line (bound-bound) transitions. If the ejecta contains lanthanide or actinide nuclei ($A \gtrsim 145$), then the optical opacity is very high $\kappa \gtrsim 10\text{--}100 \text{ cm}^2 \text{ g}^{-1}$ due to the complex atomic structure of the f-shell valence electrons of these elements, resulting in a dense forest of lines at optical/UV wavelengths (140, 141). On the other hand, ejecta containing only lighter *r*-process elements ($A \lesssim 145$) with d-shell valence electrons will possess a lower opacity, $\kappa \gtrsim 1 \text{ cm}^2 \text{ g}^{-1}$. Experimental data is unfortunately not available on most of the required line transitions, while theoretical atomic structure models solving the many-body problem are statistical in nature. The wavelength- and composition-dependent opacity of partially ionized *r*-process nuclei remains among the biggest uncertainties in modeling kilonovae.

For values of $M_{\text{ej}} \sim 10^{-2} M_{\odot}$ and $v \sim 0.1 c$ characteristic of the merger ejecta (Fig. 5), we find that $t_{\text{pk}} \approx 1\text{--}10$ days, depending on κ . The peak luminosity is determined by the radioactive heating rate, $\dot{E}_{\text{nuc}} = M \dot{\epsilon}_{\text{nuc}}$, on timescales of $t \sim t_{\text{pk}}$, where $\dot{\epsilon}_{\text{nuc}}$ is the specific radioactive heating rate. The time dependence is a power-law due to overlapping contributions of many decaying nuclei. Radioactive energy is released in three channels (136): (a) the kinetic energy of beta decay electrons and fission fragments, (b) neutrinos, (c) gamma-rays. Although particle kinetic energy can be efficiently shared with the plasma through Coulomb collisions, neutrinos escape from the system and contribute no heating. Gamma-rays may be trapped and deposit their energy at early times $t \ll t_{\text{pk}}$, but are likely to escape at later times due to their lower opacity. On timescales of days after the merger, $\dot{\epsilon}_{\text{nuc}} \approx \epsilon_{\text{th}} 10^{10} (t/\text{day})^{-1.3} \text{ erg s}^{-1} \text{ g}^{-1}$, relatively independent of $Y_e \sim 0.1\text{--}0.3$ [e.g., (136, 139)], where $\epsilon_{\text{th}} < 1$ accounts for the thermalization efficiency. The peak luminosity of the kilonova is thus approximately given by

$$L_{\text{pk}} \approx M \dot{\epsilon}_{\text{nuc}}(t_{\text{pk}}) \approx 5 \times 10^{40} \text{ erg s}^{-1} \epsilon_{\text{th}} \left(\frac{M}{10^{-2} M_{\odot}} \right)^{0.35} \left(\frac{v}{0.1 c} \right)^{0.65} \left(\frac{\kappa}{\text{cm}^2 \text{ g}^{-1}} \right)^{-0.65}, \quad (8)$$

and the effective temperature of the emission near its peak by

$$T_{\text{pk}} = \left(\frac{L_{\text{pk}}}{4\pi\sigma R_{\text{pk}}^2} \right)^{1/4} \approx 3460 \text{ K} \epsilon_{\text{th}}^{1/4} \left(\frac{M}{10^{-2} M_{\odot}} \right)^{-0.17} \left(\frac{v}{0.1 c} \right)^{-0.09} \left(\frac{\kappa}{\text{cm}^2 \text{ g}^{-1}} \right)^{-0.41}, \quad (9)$$

where $R_{\text{pk}} = vt_{\text{pk}}$. For $\kappa \gtrsim 10 \text{ cm}^2 \text{ g}^{-1}$, characteristic of lanthanide-rich ejecta, the low temperature of $T_{\text{pk}} \sim 1000 \text{ K}$ implies a spectral peak in the near-IR (142).

A candidate kilonova was discovered following the SGRB 130603B (72, 73) based on the discovery 10 days after the burst of $1\mu\text{m}$ emission in excess of that predicted by an extrapolation of the power-law synchrotron afterglow emission. Reproducing the peak luminosity of this event requires the ejection of $\sim 0.02\text{--}0.1 M_{\odot}$ of heavy *r*-process nuclei. A clearer confirmation of kilonova emission in future events would require obtaining a spectrum and identifying atomic absorption or emission lines from *r*-process elements. The velocity of the dynamical ejecta is sufficiently high that lines will be Doppler-broadened, making them

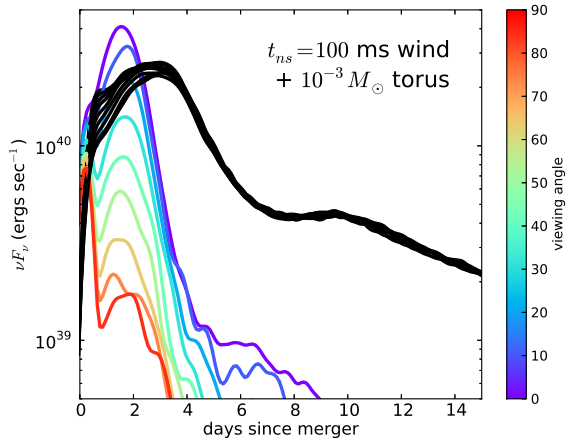


Figure 6

Kilonova light curves for a composite ejecta including a lanthanide-poor disk wind from a HMNS remnant with lifetime 100 ms, and a lanthanide-rich torus of dynamical ejecta. Colored curves show the optical light curves as a function of observer inclination from the rotation axis, while black curves show near infrared emission. Figure from Kasen et al. (143).

challenging to detect. However, the slower disk outflows may give rise to detectable narrow lines (143).

5.2.1. Early Blue Emission. The low effective temperatures of kilonovae with lanthanide-rich ejecta are a mixed blessing for GW follow-up. On one hand, their extremely red colors render them easily distinguishable from other astrophysical sources like supernovae. On the other hand, their discovery in the first place becomes much more challenging because most EM follow-up facilities are sensitive at optical wavelengths. The accretion disk outflows (§4.2.3) or shock-heated dynamical ejecta (62), in the case of a long-lived HMNS, can have a higher electron fraction and be in some cases lanthanide-free. This could in principle produce both an early ‘blue’ (visual wavelength) phase of emission lasting ~ 1 day, as well as a later ‘red’ (infrared wavelength) phase lasting ~ 1 week. The relative fluxes of the blue and red emission components would depend on the lifetime of the HMNS prior to collapsing into a black hole (116), as well as on the observer viewing angle (143) (**Figure 6**).

5.3. Fast Ejecta and the Neutron Precursor

Most of the dynamical ejecta in NSNS mergers remains sufficiently dense during its expansion that all neutrons are captured into nuclei during the r-process. However, (49) found that a few percent of the ejected mass, originating from the collision interface, expands sufficiently rapidly that neutrons avoid being captured into nuclei (r-process freeze-out).

These fast expanding free neutrons can have a dramatic impact on the kilonova emission because they reside in the outermost layers of the ejecta. Their beta decays power a luminous ‘precursor’ to the main kilonova emission, which peaks within hours following the merger (137, 144). The neutron precursor may encode information on the properties of the merging binary (e.g. NSNS versus NSBH) and the NS EOS. Future work is necessary to

assess the robustness of the fast-expanding ejecta (thus far seen with only one numerical code) and to assess the survival of the neutrons in the face of leptonizing weak interactions. The fast expanding matter could also give rise to a broadband non-thermal signature via its shock interaction with the ambient medium (145).

5.4. Non-Radioactive Energy Sources

Kilonovae can in principle be powered by more than just radioactivity, making them brighter and easier to detect. One possible heating source is shocks within the ejecta, for example if a late-time outflow from the central engine were to collide with the expanding ejecta [(146), §4.1.3]. A long-lived or stable NS remnant could also deposit its rotational energy behind the ejecta via magnetic dipole radiation (eq. 1), forming the equivalent of a young pulsar wind nebula [e.g., (147, 148, 149)]. This additional power can enhance the kilonova luminosity by up to several orders of magnitude, if the NS remnant possesses a dipole magnetic field of $B_d \sim 10^{14} - 10^{15}$ G.

5.5. Radio Transient from Ejecta Interaction with the Interstellar Medium

Matter ejected during the merger slows down as it sweeps up gas in the surrounding interstellar medium. This deceleration is mediated by the forward shock, which accelerates electrons to relativistic velocities and produces non-thermal radio synchrotron emission (150).

The ejecta transfer their energy to the ambient medium of density n at the characteristic radius (R_{dec}) at which point they have swept up a mass comparable to their own rest mass, $R_{\text{dec}} \approx (3E_K/2\pi n m_p v^2)^{1/3}$, where $E_K = Mv^2/2 \approx 10^{50} (M/0.01M_\odot)(v/0.1c)^2$ erg is the ejecta kinetic energy. This occurs at the deceleration timescale,

$$t_{\text{dec}} \approx R_{\text{dec}}/v \approx 2.5 \text{ yr} \left(\frac{E_K}{10^{50} \text{ erg}} \right)^{1/3} \left(\frac{n}{\text{cm}^{-3}} \right)^{-1/3} \left(\frac{v}{0.3c} \right)^{-5/3}, \quad (10)$$

which sets the peak timescale of the radio emission. If the observing frequency ν is located above both the synchrotron peak frequency and the self-absorption frequency, then the peak brightness for a source at distance D is achieved at t_{dec} , and is given by (150):

$$F_{\nu, \text{dec}} \approx 0.08 \text{ mJy} \left(\frac{E_K}{10^{50} \text{ erg}} \right) \left(\frac{n}{\text{cm}^{-3}} \right)^{0.83} \epsilon_{e,-1}^{1.3} \epsilon_{B,-2}^{0.83} \left(\frac{v}{0.3c} \right)^{2.3} \left(\frac{D}{200 \text{ Mpc}} \right)^{-2} \left(\frac{\nu}{\text{GHz}} \right)^{-0.65}, \quad (11)$$

where we have made the standard assumption that electrons are accelerated near the shock into a power-law energy distribution, $N(E) \propto E^{-p}$ with $p = 2.3$ above a minimum Lorentz factor of $\gamma_m \sim 2$, and that $\epsilon_B = 0.01 \epsilon_{B,-2}$ and $\epsilon_e = 0.1 \epsilon_{e,-1}$ are the fractions of post-shock energy density in the magnetic field and the power-law electrons, respectively.

Equation (11) shows that the radio brightness is greatest for high ejecta velocity and high external densities. A high value of $n \sim 0.1 - 1 \text{ cm}^{-3}$ is expected if the merger occurs in the disk of its host galaxy, but n could be much lower if the merger occurs outside of its host due to the natal NS birth kicks, or in a globular cluster. A low external density also increases the rise time to $\sim t_{\text{dec}} \gtrsim$ decade, making it challenging to uniquely associate the radio transient with a GW event.

FUTURE ISSUES

1. Precursor emission will be challenging to detect, due to its relatively low luminosity and short rise time. A coherent burst of radio emission from the NS magnetosphere orbiting through the conducting companion, while among the most promising observationally, is also the most challenging to predict theoretically.
2. The detection of one or more GW sources will help constrain the NSNS/NSBH merger rate, which in turn will constrain the contribution of mergers to the Galactic r -process sources. A GW detection can also prove the existence of NSBH binaries, none of which has been directly observed yet.
3. r -process nucleosynthesis predictions, which at present rely mostly on theoretically computed nuclear properties, will greatly benefit from new rare isotope facilities such as FRIB. Conversely, better theoretical models for the various ejecta components (e.g., tidal versus shock-driven dynamical ejecta, neutrino versus viscously-driven disk wind ejecta) can direct study towards relevant regions of parameter space to be probed by these experiments.
4. One of the biggest uncertainties in current kilonova models is the optical opacity of r -process elements in low ionization states, in particular of the Lanthanides and Actinides, for which experimental data is extremely limited. Improvements in this area would enable more accurate predictions for the color and spectral line signatures of kilonovae.
5. The ability to detect the kilonova after a GW burst is sensitive to the presence of visual wavelength emission hours to days after the merger, which in turn depends on the electron fraction and geometric distribution of the ejecta. Detection and follow-up capabilities will greatly improve as more optical transient surveys, such as LSST, become operational. Sensitive near-IR telescopes are needed for follow-up confirmation and characterization. Kilonova spectroscopy represents a promising target for planned thirty meter class telescopes.
6. Numerical simulations of NSNS/NSBH mergers will continue to improve their physical realism. Dynamical simulations need to combine MHD and neutrino transport with full GR to provide accurate estimates of the time to BH formation, the amount of mass dynamically ejected, and the mass in the accretion disk, in addition to better GW waveforms. The possible onset of a GRB jet is another major research direction. Post-merger models need to improve the treatment of angular momentum transport, including MHD, and the treatment of neutrinos, to improve the inputs for nucleosynthesis calculations and the computation of the EM signal

ACKNOWLEDGMENTS

We thank Francois Foucart and Edo Berger for helpful comments on the manuscript. RF acknowledges support from the University of California Office of the President, and from NSF grant AST-1206097. BDM gratefully acknowledges support from NASA Fermi grant NNX14AQ68G, NSF grant AST-1410950, NASA ATP grant NNX16AB30G, and the Alfred P. Sloan Foundation.

LITERATURE CITED

1. Taylor JH, Weisberg JM. *ApJ* 345:434 (1989)
2. Lyne AG, et al. *Science* 303:1153 (2004)
3. Harry GM, LIGO Scientific Collaboration. *Classical and Quantum Gravity* 27:084006 (2010)
4. Degallaix J, et al. 2013. In *9th LISA Symposium*, eds. G Auger, P Binétruy, E Plagnol, vol. 467 of *Astronomical Society of the Pacific Conference Series*
5. Somiya K. *Classical and Quantum Gravity* 29:124007 (2012)
6. Abadie J, et al. *Classical and Quantum Gravity* 27:173001 (2010)
7. Lehner L, Pretorius F. *ARA&A* 52:661 (2014)
8. Singer LP, et al. *ApJ* 795:105 (2014)
9. Ivezić v, et al. *preprint, arXiv:0805.2366* (2008)
10. van Haarlem MP, et al. *A&A* 556:A2 (2013)
11. Burbidge EM, Burbidge GR, Fowler WA, Hoyle F. *Reviews of Modern Physics* 29:547 (1957)
12. Cameron AGW. *Chalk River Report CRL-41* (1957)
13. Nuclear Science Advisory Committee. Washington, D. C.: DOE Office of Science, 1st ed. (2015)
14. Bollen G. *AIP Conference Proceedings* 1224:432 (2010)
15. Price DJ, Rosswog S. *Science* 312:719 (2006)
16. Lee WH, Ramirez-Ruiz E. *New Journal of Physics* 9:17 (2007)
17. Berger E. *ARA&A* 52:43 (2014)
18. Rosswog S. *International Journal of Modern Physics D* 24:30012 (2015)
19. Swiggum JK, et al. *ApJ* 805:156 (2015)
20. Kalogera V, et al. *ApJL* 614:L137 (2004)
21. Kim C, Perera BBP, McLaughlin MA. *MNRAS* 448:928 (2015)
22. Postnov KA, Yungelson LR. *Living Reviews in Relativity* 17:3 (2014)
23. Belczynski K, et al. *ApJS* 174:223 (2008)
24. Dominik M, et al. *ApJ* 806:263 (2015)
25. Grindlay J, Portegies Zwart S, McMillan S. *Nature Physics* 2:116 (2006)
26. Samsing J, MacLeod M, Ramirez-Ruiz E. *ApJ* 784:71 (2014)
27. O'Leary RM, Kocsis B, Loeb A. *MNRAS* 395:2127 (2009)
28. East WE, Pretorius F, Stephens BC. *Phys. Rev. D* 85:124009 (2012)
29. Vietri M. *ApJL* 471:L95 (1996)
30. Hansen BMS, Lyutikov M. *MNRAS* 322:695 (2001)
31. McWilliams ST, Levin J. *ApJ* 742:90 (2011)
32. Palenzuela C, et al. *Physical Review Letters* 111:061105 (2013)
33. Lai D. *ApJL* 757:L3 (2012)
34. Contopoulos I, Kazanas D, Fendt C. *ApJ* 511:351 (1999)
35. Thornton D, et al. *Science* 341:53 (2013)
36. Tsang D, et al. *Physical Review Letters* 108:011102 (2012)
37. Duez MD. *Classical and Quantum Gravity* 27:114002 (2010)
38. Shibata M, Taniguchi K. *Living Reviews in Relativity* 14:6 (2011)
39. Faber JA, Rasio FA. *Living Reviews in Relativity* 15:8 (2012)
40. Bauswein A, Goriely S, Janka HT. *ApJ* 773:78 (2013)
41. Gold R, et al. *PRD* 86:121501 (2012)
42. Foucart F. *PRD* 86:124007 (2012)
43. Stephens BC, East WE, Pretorius F. *ApJL* 737:L5 (2011)
44. Giacomazzo B, Rezzolla L, Baiotti L. *PRD* 83:044014 (2011)
45. Obergaulinger M, Aloy MA, Müller E. *A&A* 515:A30 (2010)
46. Kaplan JD, et al. *ApJ* 790:19 (2014)
47. Shibata M, Uryū Kō. *PRD* 61:064001 (2000)
48. Hotokezaka K, et al. *Phys. Rev. D* 83:124008 (2011)

49. Bauswein A, Baumgarte TW, Janka HT. *Physical Review Letters* 111:131101 (2013)
50. Shibata M, Taniguchi K, Uryū K. *PRD* 71:084021 (2005)
51. Duez MD, et al. *Physical Review Letters* 96:031101 (2006)
52. Siegel DM, Ciolfi R, Harte AI, Rezzolla L. *PRD* 87:121302 (2013)
53. Ruffert M, Janka HT, Schaefer G. *A&A* 311:532 (1996)
54. Paschalidis V, Etienne ZB, Shapiro SL. *Phys. Rev. D* 86:064032 (2012)
55. Sekiguchi Y, Kiuchi K, Kyutoku K, Shibata M. *Physical Review Letters* 107:051102 (2011)
56. Bauswein A, Janka HT. *Physical Review Letters* 108:011101 (2012)
57. Hotokezaka K, et al. *Phys. Rev. D* 87:024001 (2013)
58. Kyutoku K, et al. *PRD* 92:044028 (2015)
59. Oechslin R, Janka HT, Marek A. *A&A* 467:395 (2007)
60. Rezzolla L, et al. *ApJL* 732:L6 (2011)
61. Foucart F, et al. *PRD* 90:024026 (2014)
62. Wanaajo S, et al. *ApJ* 789:L39 (2014)
63. Foucart F, et al. *Phys. Rev. D.* 91:124021 (2015)
64. Hotokezaka K, et al. *PRD* 88:044026 (2013)
65. Oechslin R, Janka HT. *MNRAS* 368:1489 (2006)
66. Ruffert M, Janka HT. *A&A* 344:573 (1999)
67. Woosley SE, Bloom JS. *ARA&A* 44:507 (2006)
68. Paczynski B. *ApJ* 308:L43 (1986)
69. Eichler D, Livio M, Piran T, Schramm DN. *Nature* 340:126 (1989)
70. Belczynski K, et al. *ApJ* 648:1110 (2006)
71. Fong W, Berger E. *ApJ* 776:18 (2013)
72. Tanvir NR, et al. *Nature* 500:547 (2013)
73. Berger E, Fong W, Chornock R. *ApJ* 774:L23 (2013)
74. Dermer CD, Atoyan A. *ApJL* 643:L13 (2006)
75. Margalit B, Metzger BD, Beloborodov AM. *Physical Review Letters* 115:171101 (2015)
76. Goodman J. *ApJ* 308:L47 (1986)
77. Murguia-Berthier A, et al. *ApJL* 788:L8 (2014)
78. Just O, et al. *ApJL*, submitted, *arXiv:1510.04288* (2015)
79. Blandford RD, Znajek RL. *MNRAS* 179:433 (1977)
80. Kiuchi K, et al. *Phys. Rev. D.* 90:041502 (2014)
81. Paschalidis V, Ruiz M, Shapiro SL. *ApJ* 806:L14 (2015)
82. Aloy MA, Janka HT, Müller E. *A&A* 436:273 (2005)
83. Bucciantini N, Metzger BD, Thompson TA, Quataert E. *MNRAS* 419:1537 (2012)
84. Nagakura H, et al. *ApJL* 784:L28 (2014)
85. Norris JP, Bonnell JT. *ApJ* 643:266 (2006)
86. Rowlinson A, et al. *MNRAS* 430:1061 (2013)
87. Rosswog S. *MNRAS* 376:L48 (2007)
88. Lee WH, Ramirez-Ruiz E, López-Cámara D. *ApJ* 699:L93 (2009)
89. Kisaka S, Ioka K. *ApJL* 804:L16 (2015)
90. Fernández R, et al. *MNRAS* 449:390 (2015)
91. Antoniadis J, et al. *Science* 340:448 (2013)
92. Özel F, et al. *ApJ* 724:L199 (2010)
93. Giacomazzo B, Perna R. *ApJL* 771:L26 (2013)
94. Duncan RC, Thompson C. *ApJ* 392:L9 (1992)
95. Dessart L, et al. *ApJ* 690:1681 (2009)
96. Popham R, Woosley SE, Fryer C. *ApJ* 518:356 (1999)
97. Narayan R, Yi I. *ApJ* 428:L13 (1994)
98. Chen WX, Beloborodov AM. *ApJ* 657:383 (2007)
99. Metzger BD, Piro AL, Quataert E. *MNRAS* 390:781 (2008)

100. Metzger BD, Piro AL, Quataert E. *MNRAS* 396:304 (2009)
101. Lee WH, Ramirez-Ruiz E. *ApJ* 577:893 (2002)
102. Lee WH, Ramirez-Ruiz E, Page D. *ApJ* 608:L5 (2004)
103. Setiawan S, Ruffert M, Janka HT. *A&A* 458:553 (2006)
104. Shibata M, Sekiguchi YI, Takahashi R. *Progress of Theoretical Physics* 118:257 (2007)
105. Shibata M, Sekiguchi Y. *Progress of Theoretical Physics* 127:535 (2012)
106. Ruffert M, Janka HT, Takahashi K, Schaefer G. *A&A* 319:122 (1997)
107. Scholberg K. *ARNPS* 62:81 (2012)
108. Duncan RC, Shapiro SL, Wasserman I. *ApJ* 309:141 (1986)
109. Surman R, et al. *ApJ* 679:L117 (2008)
110. Metzger BD, Thompson TA, Quataert E. *ApJ* 676:1130 (2008)
111. Wanajo S, Janka HT. *ApJ* 746:180 (2012)
112. Fernández R, Metzger BD. *MNRAS* 435:502 (2013)
113. Just O, et al. *MNRAS* 448:541 (2015)
114. Richers S, et al. *ApJ* 813:38 (2015)
115. Perego A, et al. *MNRAS* 443:3134 (2014)
116. Metzger BD, Fernández R. *MNRAS* 441:3444 (2014)
117. Kohri K, Narayan R, Piran T. *ApJ* 629:341 (2005)
118. Arnould M, Goriely S, Takahashi K. *Phys. Rep.* 450:97 (2007)
119. Sneden C, Cowan JJ, Gallino R. *ARA&A* 46:241 (2008)
120. Mumpower MR, Surman R, McLaughlin GC, Aprahamian A. *preprint, arXiv:1508.07352* (2015)
121. Metzger BD, Berger E. *ApJ* 746:48 (2012)
122. Meyer BS, et al. *ApJ* 399:656 (1992)
123. Cameron AGW. *ApJ* 562:456 (2001)
124. Epstein RI, Colgate SA, Haxton WC. *PRL* 61:2038 (1988)
125. Lattimer JM, Schramm DN. *ApJ* 192:L145 (1974)
126. Freiburghaus C, Rosswog S, Thielemann F. *ApJ* 525:L121 (1999)
127. Goriely S, et al. *Nuclear Physics A* 758:587 (2005)
128. Eichler M, et al. *ApJ* 808:30 (2015)
129. Goriely S, Bauswein A, Janka HT. *ApJ* 738:L32 (2011)
130. Korobkin O, Rosswog S, Arcones A, Winteler C. *MNRAS* 426:1940 (2012)
131. Martin D, et al. *ApJ* 813:2 (2015)
132. van de Voort F, et al. *MNRAS* 447:140 (2015)
133. Shen S, et al. *ApJ* 807:115 (2015)
134. Hirai Y, et al. *ApJ* 814:41 (2015)
135. Arcones A, Montes F. *ApJ* 731:5 (2011)
136. Metzger BD, et al. *MNRAS* 406:2650 (2010)
137. Kulkarni SR. *preprint, arXiv:astro-ph/0510256* (2005)
138. Li LX, Paczyński B. *ApJL* 507:L59 (1998)
139. Roberts LF, Kasen D, Lee WH, Ramirez-Ruiz E. *ApJ* 736:L21 (2011)
140. Kasen D, Badnell NR, Barnes J. *ApJ* 774:25 (2013)
141. Tanaka M, Hotokezaka K. *ApJ* 775:113 (2013)
142. Barnes J, Kasen D. *ApJ* 775:18 (2013)
143. Kasen D, Fernández R, Metzger BD. *MNRAS* 450:1777 (2015)
144. Metzger BD, Bauswein A, Goriely S, Kasen D. *MNRAS* 446:1115 (2015)
145. Kyutoku K, Ioka K, Shibata M. *MNRAS* 437:L6 (2014)
146. Kisaka S, Ioka K, Takami H. *ApJ* 802:119 (2015)
147. Yu YW, Zhang B, Gao H. *ApJL* 776:L40 (2013)
148. Metzger BD, Piro AL. *MNRAS* 439:3916 (2014)
149. Siegel DM, Ciolfi R. *preprint, arXiv:1508.07939* (2015)

150. Nakar E, Piran T. *Nature* 478:82 (2011)